

All-optical amplitude-phase transmultiplexing of RZ-OOK and RZ-BPSK to RZ-QPSK by polarization-insensitive XPM using a nonlinear birefringent AlGaAs waveguide

B. M. Cannon,^{1,2,3,*} T. Mahmood,^{1,2,3} W. Astar,^{1,2} P. Apiratikul,¹ G. Porkolab,¹ P. Boudra III,³ T. Mohsenin,³ C. J. K. Richardson,¹ and G. M. Carter^{1,2,3}

¹Laboratory for Physical Sciences (LPS), 8050 Greenmead Drive, College Park, Maryland 20740, USA

²Center for Advanced Studies in Photonics Research (CASPR), 1000 Hilltop Circle, Baltimore, Maryland 21250, USA

³Department of Computer Science and Electrical Engineering, University of Maryland, Baltimore County (UMBC), 1000 Hilltop Circle, Baltimore, Maryland 21250, USA

*bcannon1@lps.umd.edu

Abstract: Polarization-insensitive (PI) phase-transmultiplexing (PTM) of a 10-Gb/s return-to-zero ON-OFF keying (RZ-OOK) pump and a 10-Gb/s RZ-binary phase-shift keying (RZ-BPSK) probe to 20-Gb/s RZ-quadrature-PSK (RZ-QPSK) has been successfully demonstrated for the first time in a passive, birefringent AlGaAs waveguide, utilizing PI cross-phase modulation (PI-XPM). For differential QPSK (DQPSK)-detection, a 10^{-9} -BER pre-amplified receiver sensitivity penalty of ≈ 2.5 dB for the in-phase component and ≈ 4.9 dB for the quadrature component were found. The penalties were relative to the FPGA-precoded RZ-DQPSK baseline for a pump-probe detuning of ≈ 12 nm, when the probe state of polarization was scrambled and the pump was launched off-axis into the waveguide.

©2013 Optical Society of America

OCIS codes: (190.4390) Nonlinear optics, integrated optics; (190.4360) Nonlinear optics, devices.

References and links

1. K. Inoue, "Polarization independent wavelength conversion using fiber four-wave mixing with two orthogonal pump lights of different frequencies," *J. Lightwave Technol.* **12**(11), 1916–1920 (1994).
2. T. Hasegawa, K. Inoue, and K. Oda, "Polarization independent frequency conversion by fiber four-wave mixing with a polarization diversity technique," *IEEE Photon. Technol. Lett.* **5**(8), 947–949 (1993).
3. K. K. Chow, C. Shu, C. Lin, and A. Bjarklev, "Polarization-insensitive widely tunable wavelength converter based on four-wave mixing in a dispersion-flattened nonlinear photonic Crystal fiber," *IEEE Photon. Technol. Lett.* **17**(3), 624–626 (2005).
4. T. Yang, C. Shu, and C. Lin, "Depolarization technique for wavelength conversion using four-wave mixing in a dispersion-flattened photonic crystal fiber," *Opt. Express* **13**(14), 5409–5415 (2005).
5. J. Li, A. Berntson, and G. Jacobsen, "Polarization-independent optical demultiplexing using XPM-induced wavelength shifting in highly nonlinear fiber," *IEEE Photon. Technol. Lett.* **20**(9), 691–693 (2008).
6. T. Tanemura, J. Suzuki, K. Katoh, and K. Kikuchi, "Polarization-insensitive all-optical wavelength conversion using cross-phase modulation in twisted fiber and optical filtering," *IEEE Photon. Technol. Lett.* **17**(5), 1052–1054 (2005).
7. A. S. Lenihan, R. Salem, T. E. Murphy, and G. M. Carter, "All-optical 80-gb/s time-division demultiplexing using polarization-insensitive cross-phase modulation in photonic crystal fiber," *IEEE Photon. Technol. Lett.* **18**(12), 1329–1331 (2006).
8. A. S. Lenihan and G. M. Carter, "Polarization-insensitive wavelength conversion at 40 Gb/s using birefringent nonlinear fiber," in *Lasers and Electro-Optics, 2007. CLEO 2007. Conference On* (2007), pp. 1–2.
9. W. Astar, C.-C. Wei, Y.-J. Chen, J. Chen, and G. M. Carter, "Polarization-insensitive, 40 Gb/s wavelength and RZ-OOK-to-RZ-BPSK modulation format conversion by XPM in a highly nonlinear PCF," *Opt. Express* **16**(16), 12039–12049 (2008).

10. B. M. Cannon, W. Astar, T. Mahmood, P. Apiratikul, G. A. Porkolab, C. J. K. Richardson, and G. M. Carter, "Data transfer from RZ-OOK to RZ-BPSK by polarization-insensitive XPM in a passive birefringent nonlinear AlGaAs waveguide," *J. Lightwave Technol.* **31**(6), 952–966 (2013).
11. H. Hu, E. Palushani, M. Galili, H. C. H. Mulvad, A. Clausen, L. K. Oxenløwe, and P. Jeppesen, "640 Gbit/s and 1.28 Tbit/s polarisation insensitive all optical wavelength conversion," *Opt. Express* **18**(10), 9961–9966 (2010).
12. M. Pu, H. Hu, C. Peucheret, H. Ji, M. Galili, L. K. Oxenløwe, P. Jeppesen, J. M. Hvam, and K. Yvind, "Polarization insensitive wavelength conversion in a dispersion-engineered silicon waveguide," *Opt. Express* **20**(15), 16374–16380 (2012).
13. W. Astar, J. B. Driscoll, X. Liu, J. I. Dadap, W. M. J. Green, Y. Vlasov, G. M. Carter, and R. M. Osgood, "Tunable wavelength conversion by XPM in a silicon nanowire, and the potential for XPM-multicasting," *J. Lightwave Technol.* **28**(17), 2499–2511 (2010).
14. W. Astar, J. B. Driscoll, X. Liu, J. I. Dadap, W. M. J. Green, Y. A. Vlasov, G. M. Carter, and R. M. Osgood, "Conversion of 10 Gb/s NRZ-OOK to RZ-OOK utilizing XPM in a Si nanowire," *Opt. Express* **17**(15), 12987–12999 (2009).
15. S. Gao, X. Zhang, Z. Li, and S. He, "Polarization-independent wavelength conversion using an angled-polarization pump in a silicon nanowire waveguide," *IEEE J. Quantum Electron.* **16**(1), 250–256 (2010).
16. J. B. Driscoll, W. Astar, X. Liu, J. I. Dadap, W. M. J. Green, Y. A. Vlasov, G. M. Carter, and R. M. Osgood, "All-optical wavelength conversion of 10 Gb/s RZ-OOK data in a silicon nanowire via cross-phase modulation: experiment and theoretical investigation," *IEEE J. Quantum Electron.* **16**(5), 1448–1459 (2010).
17. M. Dinu, F. Quochi, and H. Garcia, "Third-order nonlinearities in silicon at telecom wavelengths," *Appl. Phys. Lett.* **82**(18), 2954–2956 (2003).
18. H. Hu, H. Ji, M. Galili, M. Pu, C. Peucheret, H. Christian H Mulvad, K. Yvind, J. M. Hvam, P. Jeppesen, and L. K. Oxenløwe, "Ultra-high-speed wavelength conversion in a silicon photonic chip," *Opt. Express* **19**(21), 19886–19894 (2011).
19. S. Gehrsitz, F. K. Reinhardt, C. Gourgon, N. Herres, A. Vonlanthen, and H. Sigg, "The refractive index of $\text{Al}_x\text{Ga}_{(1-x)}\text{As}$ below the band gap: accurate determination and empirical modeling," *J. Appl. Phys.* **87**(11), 7825–7837 (2000).
20. J. U. Kang, G. I. Stegeman, A. Villeneuve, and J. S. Aitchison, "AlGaAs below half bandgap: a laboratory for spatial soliton physics," *Pure and Appl. Opt.: J. European Opt. Society Part A* **5**, 583–594 (1996).
21. J. S. Aitchison, D. C. Hutchings, J. U. Kang, G. I. Stegeman, and A. Villeneuve, "The nonlinear optical properties of AlGaAs at the half band gap," *IEEE J. Quantum Electron.* **33**(3), 341–348 (1997).
22. K. Dolgaleva, W. C. Ng, L. Qian, and J. S. Aitchison, "Compact highly-nonlinear AlGaAs waveguides for efficient wavelength conversion," *Opt. Express* **19**(13), 12440–12455 (2011).
23. K. Dolgaleva, W. C. Ng, L. Qian, J. S. Aitchison, M. C. Camasta, and M. Sorel, "Broadband self-phase modulation, cross-phase modulation, and four-wave mixing in 9-mm-long AlGaAs waveguides," *Opt. Lett.* **35**(24), 4093–4095 (2010).
24. W. Astar, P. Apiratikul, T. E. Murphy, and G. M. Carter, "Wavelength conversion of 10-Gb/s RZ-OOK using filtered XPM in a passive GaAs-AlGaAs waveguide," *IEEE Photon. Technol. Lett.* **22**(9), 637–639 (2010).
25. W. Astar, P. Apiratikul, B. M. Cannon, T. Mahmood, J. J. Wathen, J. V. Hryniewicz, S. Kanakaraju, C. J. K. Richardson, T. E. Murphy, and G. M. Carter, "Conversion of RZ-OOK to RZ-BPSK by XPM in a passive AlGaAs waveguide," *IEEE Photon. Technol. Lett.* **23**(19), 1397–1399 (2011).
26. J. J. Wathen, P. Apiratikul, B. M. Cannon, T. Mahmood, W. Astar, C. J. K. Richardson, G. A. Porkolab, G. M. Carter, and T. E. Murphy, "Efficient continuous-wave four-wave mixing and self-phase modulation in a bandgap-engineered AlGaAs waveguide," in *CLEO: Science and Innovations, OSA Technical Digest (online)* (Optical Society of America, 2012), Paper CW1A.4. (2012).
27. M. Galili, C. Schmidt-Langhorst, R. Ludwig, F. Futami, S. Watanabe, and C. Schubert, "All-optical combination of DPSK and OOK to 160 Gbit/s DQPSK data signals," in *Conference on Optical Fiber Communication and the National Fiber Optic Engineers Conference* (2007), pp. 1–3.
28. E. Kapon and R. Bhat, "Low loss single mode GaAs/AlGaAs optical waveguides grown by organometallic vapor phase epitaxy," *Appl. Phys. Lett.* **50**(23), 1628–1630 (1987).
29. A. B. Fallahkhair, K. S. Li, and T. E. Murphy, "Vector finite difference modesolver for anisotropic dielectric waveguides," *J. Lightwave Technol.* **26**(11), 1423–1431 (2008).
30. A. Villeneuve, C. C. Yang, P. G. J. Wigley, G. I. Stegeman, J. S. Aitchison, and C. N. Ironside, "Ultrafast all optical switching in semiconductor nonlinear directional couplers at half the band gap," *Appl. Phys. Lett.* **61**(2), 147–149 (1992).
31. G. P. Agrawal, *Nonlinear Fiber Optics*, 3rd ed. (Academic Press, 2001).
32. P. J. Winzer and A. Kalmar, "Sensitivity enhancement of optical receivers by impulsive coding," *J. Lightwave Technol.* **17**(2), 171–177 (1999).
33. P. Humblet and M. Azizoglu, "On the bit error rate of lightwave systems with optical amplifiers," *J. Lightwave Technol.* **9**(11), 1576–1582 (1991).
34. C. Rasmussen, T. Fjelde, J. Bennike, F. Liu, S. Dey, B. Mikkelsen, P. Mamyshev, P. Serbe, P. van der Wagt, Y. Akasaka, D. Harris, D. Gapontsev, V. Ivshin, and P. Reeves-Hall, "DWDM 40G transmission over trans-pacific distance (10 000 km) using CSRZ-DPSK, enhanced FEC, and all-Raman-amplified 100-km UltraWave fiber spans," *J. Lightwave Technol.* **22**(1), 203–207 (2004).
35. J. Proakis, *Digital Communications*, 4th ed. (McGraw-Hill Science/Engineering/Math, 2000).

36. J. M. Gene, M. Soler, R. I. Killey, and J. Prat, "Investigation of 10-Gb/s optical DQPSK systems in presence of chromatic dispersion, fiber nonlinearities, and phase noise," *IEEE Photon. Technol. Lett.* **16**(3), 924–926 (2004).
37. H. Kim and P. J. Winzer, "Robustness to laser frequency offset in direct-detection DPSK and DQPSK systems," *J. Lightwave Technol.* **21**(9), 1887–1891 (2003).
-

1. Introduction

Advances in nonlinear optical signal processing (NOSP) techniques, along with device design, have made polarization-insensitive (PI)-NOSP possible. A significant disadvantage of NOSP employing the $\chi^{(3)}$ -nonlinearity, is the strong dependence of this nonlinearity on the input signals' states of polarization (SOP), which can vary randomly in realistic systems. Several techniques have been explored to enable PI-NOSP in a variety of nonlinear devices. A technique first demonstrated by Inoue [1] reduced the polarization sensitivity of four-wave-mixing (FWM) by launching two orthogonally polarized pumps in a nonlinear medium. Other techniques utilized an external polarization diversity loop in order to reduce the polarization sensitivity [2,3]. A depolarization technique for wavelength conversion which involved the use of a pump depolarizer before a nonlinear photonic crystal fiber (PCF), was also demonstrated by Yang et al. [4]. Li et al. demonstrated PI-NOSP by using a length of polarization-maintaining fiber (PMF) at the input of a highly nonlinear fiber (HNLF) to split the pump and the probe into two orthogonally polarized components [5]. It was also found that circular birefringence could be induced in a highly nonlinear fiber by twisting the fiber, and the birefringence could be used to reduce the polarization sensitivity of NOSP [6]. Another technique, first demonstrated by Lenihan et al. [7,8], utilized the inherent birefringence of a PCF to enable PI-NOSP, which eliminated the need for a polarization diversity loop, or an external birefringence. It was discovered that by adjusting the pump launch angle to $\approx 45^\circ$ with respect to a birefringent axis of the PCF, the polarization sensitivity of the experiment could be reduced. The symmetric launch angle was due to the low polarization-dependent loss (PDL < 0.2 dB) and the isotropy of the PCF's nonlinear coefficient (γ). Moreover, an additional minimum pump-probe detuning (PPD), depending on the magnitude of the *deterministic* differential group delay (DGD) of the PCF was also required to further reduce the polarization sensitivity [9].

Several passive, birefringent devices including AlGaAs waveguides [10], PCF [9], HNLF-PMF [11], and *c*-Si [12] have recently demonstrated PI-NOSP capabilities. Conventionally undesirable propagation impairments such as XPM, FWM, and dispersion are exploited in these specially designed birefringent devices to enable PI-NOSP. PCF has been successfully utilized for PI-NOSP [9], but its relatively weak nonlinear properties resulting in a comparatively long length does not allow for integration in a compact platform. By contrast, semiconductor waveguides are fully capable of performing similar PI-NOSP functions as the PCF, but in much shorter device interaction lengths. Semiconductor waveguides also have potential for on-chip solid-state electronics integration [13–16]. At 1550 nm, the $\text{Al}_{0.18}\text{Ga}_{0.82}\text{As}$ waveguide has a nonlinear index of $\approx 1.6 \times 10^{-13} \text{ cm}^2/\text{W}$, which is ≈ 4 -times larger than that of *c*-Si [17]. Semiconductor waveguides have significantly higher propagation loss (> 1 dB/cm) than PCF ($\approx 10^{-4}$ dB/cm), but their stronger modal confinement (smaller effective areas) and larger Kerr index enable centimeter-long waveguides to achieve similar PI-NOSP operations as in many meters of PCF. However, two-photon absorption (TPA) is a highly undesirable nonlinear effect that accompanies the Kerr effect in semiconductor waveguides. Therefore, TPA should be minimized to avoid undesirable cross-amplitude modulation (XAM), free-carrier absorption, and free-carrier dispersion. Ultra-high-speed NOSP, such as wavelength conversion, can be performed in properly engineered Si waveguides if the coupled power to the waveguide is sufficient to achieve the desired NOSP, when it is below the TPA threshold [12, 18]. Alternatively, $\text{Al}_{0.18}\text{Ga}_{0.82}\text{As}$ waveguides allow for TPA to be mitigated by regulating the aluminum concentration during epitaxial growth to engineer the material's bandgap [19–21], but this is done at the expense of the strength of the

Kerr index (n_2). By contrast, band-gap engineering is not possible in *c*-Si waveguides, which can limit their NOSP capabilities. Consequently, AlGaAs has received much attention as a versatile medium for NOSP [10, 22–26].

Until now, phase transmultiplexing (PTM) to RZ-DQPSK via XPM was only demonstrated in a passive, highly nonlinear fiber (HNLF) by Galili et al., which utilized a copolarized OOK pump and a DPSK probe [27]. In this process, a DPSK probe was multiplexed with a phase transferred from an OOK pump via XPM to generate DQPSK; hence the term phase-transmultiplexing. The resultant DQPSK signal was composed of in-phase and quadrature components that carried the data of the original DPSK and OOK channels, respectively, before passing through the receiver. However, within probe-induced XPM and propagation loss, the RZ-OOK pump was left intact. In realistic systems, signals can have unpredictable SOPs. Although HNLF is a passive device, it lacks the sufficient deterministic DGD to enable the type of PI-NOSP demonstrated in [8,9], which may be achieved with an external birefringence, or a polarization diversity loop. However, this complicates the implementation of PTM in the low birefringence HNLF. Reported here is the first successful demonstration of PI-PTM with a 10-Gb/s RZ-OOK pump and a polarization-scrambled 10-Gb/s RZ-BPSK probe to 20-Gb/s RZ-QPSK in a passive, birefringent, Al_{0.18}Ga_{0.82}As waveguide. The performance of 20-Gb/s RZ-QPSK was quantified with a receiver sensitivity measurement using DQPSK detection, the results of which were compared with conventional, precoded DQPSK generated using a field-programmable gate-array (FPGA) based transmitter. A 10⁻⁹-BER penalty of ≈2.5 dB for the in-phase component and ≈4.9 dB for the quadrature component were found when the pump was launched off-axis into the waveguide at a pump-probe detuning of ≈12 nm, while the probe SOP was randomized.

2. Phase-transmultiplexing concept

The proposed PTM to RZ-QPSK scheme is shown in Fig. 1, where the probe is a RZ-BPSK signal and the pump is a RZ-OOK signal. After propagation in a nonlinear medium whose physical length is much smaller than the smallest dispersion length for the signals involved, and considering only XPM and self-phase modulation (SPM), the ideal phase of the probe will be given by:

$$\phi_{2\text{out}}(t) = \phi_{2\text{in}}(t) + \phi_{2\text{SPM}}(t) + \phi_{1\text{XPM}}(t) = \phi_{\text{BPSK}}(t) + \gamma L_{\text{eff}} P_2(t) + 2\gamma L_{\text{eff}} P_{\text{OOK}}(t) \quad (1)$$

The nonlinear coefficient and effective length for an on-axis launch are represented by γ and L_{eff} . The peak power of the pump or the probe is represented by P , where the subscript 1 has been assigned to the pump and 2 to the probe. The effective probe phase is a time-dependent function of the probe input phase (due to BPSK), as well as pump-induced XPM and probe-induced SPM. The bit-wise SPM phase shift is periodically identical with the probe power due to the probe's constant power envelope, and this phase shift is eliminated in a differential detection receiver that consists of a 1-bit-delay asymmetric Mach-Zehnder interferometer (AMZI). For PTM of RZ-OOK and RZ-BPSK to RZ-QPSK, the pump power should be sufficient to induce a $\pi/2$ phase shift on the probe for every occurrence of a ONE in the pump. In the process at the output of the waveguide, a 4-level RZ-QPSK signal is generated carrying the data of the input RZ-OOK and RZ-DPSK signals, as shown in Fig. 1, while leaving the RZ-OOK pump intact. The probe is subsequently isolated with an optical bandpass filter (OBPF) at the output of the waveguide.

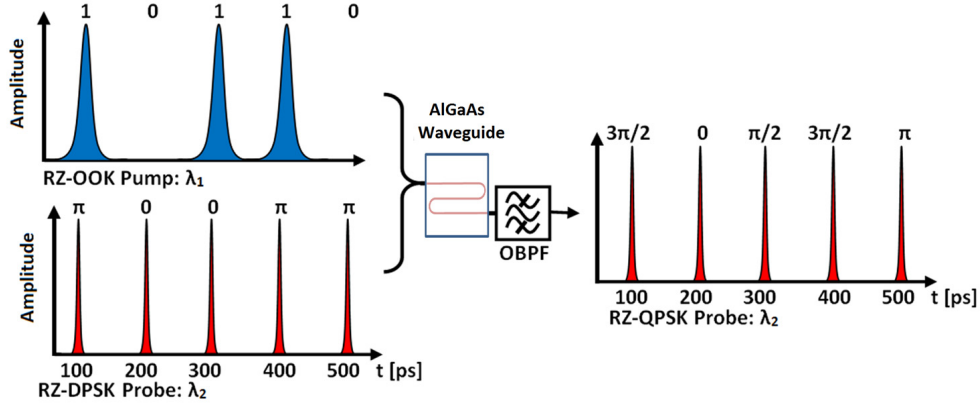


Fig. 1. Scheme for PTM to RZ-QPSK using a RZ-BPSK probe (red) and a RZ-OOK pump (blue). OBPF = optical bandpass filter.

3. Experiments and discussion

3.1 Waveguide fabrication and characterization

The epistructure of the device was grown on a n-GaAs substrate using solid-source molecular beam epitaxy. The guiding layer had an Al concentration of $\approx 18\%$, chosen to suppress TPA within the C-band. The waveguide was fabricated in the same manner described in [25], and a cross-section of the waveguide's structure, and a scanning electron micrograph (SEM) image are shown in Fig. 2. The respective propagation losses for the QTE (x -axis), and the QTM (y -axis) modes were $\alpha_x \approx 2.4$ dB/cm and $\alpha_y \approx 2$ dB/cm, measured at 1550 nm using the Fabry-Perot resonance technique outlined in [28]. To illustrate the anisotropic aspects of the waveguide, the transverse spatial distributions were estimated using the full-vector finite difference method [29].

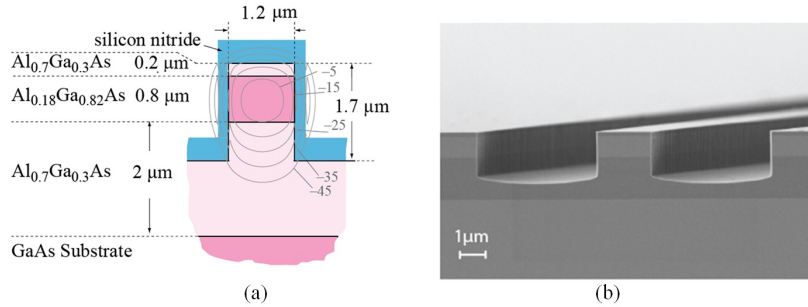


Fig. 2. (a) Cross-section of the AlGaAs waveguide, and calculated optical mode profile (showing power dB-contours). (b) SEM demonstrates the high-quality, anisotropic etch. For (a), the x -axis is taken to be parallel to the substrate, while the z -axis, into the page.

Subsequently, the nonlinear coefficients (γ) for each axis were then estimated from the $\text{Al}_{0.18}\text{Ga}_{0.82}\text{As}$ Kerr index (n_2) data presented in [30], and using [31]

$$\gamma_{\mu\nu\sigma\xi} = \frac{\omega_\mu n_{2\sigma}(\omega_\mu)}{c} \frac{\iint |F_\sigma(x, y, \omega_\mu)|^2 |F_\xi(x, y, \omega_\nu)|^2 dS}{\left(\iint |F_\sigma(x, y, \omega_\mu)|^2 dS\right) \left(\iint |F_\xi(x, y, \omega_\nu)|^2 dS\right)} = \frac{\omega_\mu n_{2\sigma}(\omega_\mu)}{c A_{\text{eff}\sigma}(\omega_\mu)} \delta_{\mu\nu} \delta_{\xi\sigma}; \quad (2)$$

$$\sigma, \xi \in \{x, y\}; \quad \mu, \nu \in \{1, 2\}$$

and the rational expression reduces to $1/A_{\text{eff}}$ but only when $\nu = \mu$ for SPM ($\xi = \sigma$), otherwise it is termed the shape factor. In Eq. (2), c is the speed of light in vacuum, $F_{\sigma}(x,y, \omega_{\mu})$ is the spatial

Table 1. Approximate Critical Parameters and Values

Quantity (symbol) [units]	Pump (1559 nm)		Probe (1547 nm)	
	QTE (x)	QTM (y)	QTE (x)	QTM (y)
Kerr Index (n_2) [cm^2/W]	1.51×10^{-13}	1.40×10^{-13}	1.57×10^{-13}	1.47×10^{-13}
Shape Factor [μm^2]	0.73	0.79	0.73	0.78
Nonlinear coefficient (γ) [$\text{W}^{-1}\text{cm}^{-1}$]	0.84	0.72	0.88	0.76
Linear loss (α) [dB/cm]	2.4	2.0	2.4	2.0
Effective Length (L_{eff}) [cm]	1.4	1.5	1.4	1.5
Gaussian FWHM pulse-width* (ΔT) [ps]	14.6		2.6	
Average Power* (\bar{P}) [dBm]	21		9	
Physical Length (L) [cm]	2.5			
DGD($\Delta\tau$) [ps]	1			

distribution of the waveguide vector mode (σ being either x or y) for the μ -th signal, and dS is the differential transverse area element. The region of integration is the cross-section of the waveguide. In general, the nonlinear coefficient depends on whether the nonlinearity is due to co-polarized ($\xi = \sigma$) or cross-polarized ($\xi \neq \sigma$) SPM ($\mu = \nu$), or to co-polarized ($\xi = \sigma$) or cross-polarized ($\xi \neq \sigma$) XPM ($\mu \neq \nu$). It is observed that the nonlinear coefficient also reflects the polarization dependence of the Kerr index, $n_{2\sigma}$. All parameters and values are summarized in Table 1, which demonstrates that the waveguide possesses significant linear and nonlinear anisotropies.

3.2 Implementation of phase-transmultiplexing (PTM)

The experimental setup for PTM by PI-XPM from 10-Gb/s RZ-OOK and 10-Gb/s RZ-BPSK to 20-Gb/s RZ-QPSK is shown in Fig. 3. The probe was a 10-Gb/s RZ-BSPK signal, 2^{11} -1 pseudo-random bit sequence (PRBS), centered at 1547 nm, with a pulse-width of ≈ 2.6 ps measured at full-width-at-half-maximum (FWHM). The probe pulses were generated using a commercially available (from Time-Bandwidth Products AG) Ergo-XG Er^{3+} -doped glass waveguide laser. The Ergo-XG laser was used because it was a transform-limited pulse-source with a pulse-width much smaller than that of the pump. The NRZ-OOK pump, which served as the locally generated signal in the experiment, was a 10 Gb/s, 2^{11} -1 PRBS signal, centered at 1559 nm and was pulse-carved using a commercially available (from Cyoptics, Inc.), Franz-Keldysh-effect electro-absorption modulator (EAM) driven simultaneously by 10 GHz and 20 GHz clock signals. The 10 GHz clock signal was recovered from the inbound RZ-BPSK probe, which served as the remotely generated signal. The EAM was biased into deep absorption near its damage threshold to generate ≈ 14.6 -ps-FWHM RZ-OOK. The NRZ-RZ pulse conversion was carried out to enhance the OOK pump peak power, and therefore its XPM-induced nonlinear phase shift in the waveguide. However, the pulse-width of the pump was chosen to be sufficiently large to ensure a nearly uniform XPM modulation over the duration of the probe pulse during the occurrence of a ONE-bit in the pump, to minimize chirp. Larger pump-probe pulse-widths could be used for the PTM operation, but further optimization of the waveguide structure is required to ensure the $\pi/2$ phase shift can be obtained without exceeding the damage threshold of the waveguide, which is close to ≈ 31 dBm average power illuminating the input facet. The pump and the probe were combined and coupled into the waveguide using a 50% 2×2 fused-silica-fiber coupler and a lensed fiber. They were temporally synchronized using an ODL. The lensed fiber beam-waist diameter was ≈ 2 μm and was located at the input plane of the waveguide with a per-facet coupling loss of ≈ 3 dB. For pump co-polarized with probe along a birefringent axis, the average pump and probe powers coupled into the waveguide using the lensed fiber were ≈ 21 dBm and ≈ 9 dBm,

respectively. Due to the low duty cycle of the probe, its optimal power in the waveguide was governed by a trade-off between minimum OSNR and receiver filtering distortion due to excessive SPM- and XPM-induced spectral broadening. The SOPs of the pump and the probe

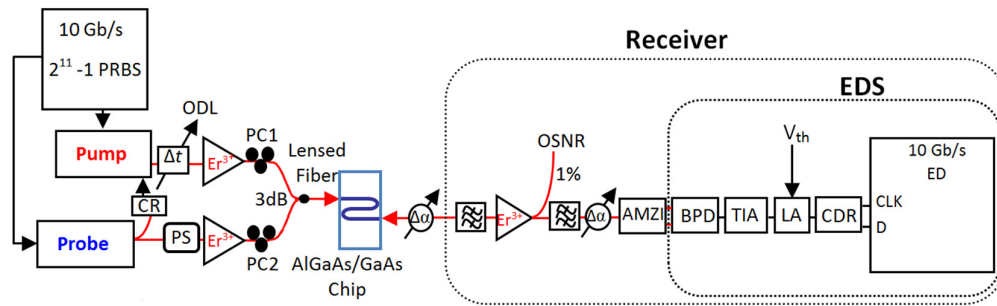


Fig. 3. Experimental setup for PTM QPSK. (ODL: optical delay line, PRBS: pseudo-random bit-sequence, ODL: optical delay line, CR: clock recovery, PS: polarization scrambler, AMZI: asymmetric Mach-Zehnder interferometer, BPD: balanced photodetector, TIA: transimpedance amplifier, LA: limiting amplifier, V_{th} : threshold voltage, CDR: clock-data recovery module, EDS: error-detector subsystem, $\Delta\alpha$: variable optical attenuator).

were individually controlled by mechanical polarization controllers (PC1 and PC2) at the input of the 50% coupler, which were used for the case of pump co-polarized with probe along a birefringent axis. The probe SOP could also be randomized at a scrambling rate > 12 kHz, by enabling the polarization scrambler (PS), shown in Fig. 3. The output of the waveguide was collected using an identical lensed fiber as that at the input, and the probe was subsequently isolated using a super-Gaussian optical-bandpass-filter (OBPF) with a FWHM of 0.6 nm, and centered at 1547 nm (the mean central wavelength of the Ergo-XG laser). XAM was considered negligible for the pump/probe powers and the filter bandwidths used in the experiment, because the waveguide's guiding layer bandgap was engineered to minimize TPA in the C-band.

Experimentally, the resultant RZ-QPSK signal (which was previously the RZ-BPSK probe at the input of the waveguide) was received as a DQPSK signal in a direct-detection receiver. The DQPSK receiver consisted of a dual-stage, high-gain low noise figure (LNF) EDFA with an inter-stage 1.4-nm-OBPF for the elimination of out-of-band ASE that could compete for the gain of the second amplification stage. The remainder of the 10 Gb/s receiver consisted of a 1-bit-delay AMZI, a BPD, a transimpedance amplifier (TIA), a limiting amplifier (LA), followed by a standard 10-Gb/s clock-data recovery (CDR) module, and an error detector (ED). The BER threshold was set by the LA. For DQPSK receiver sensitivity measurements, a variable optical attenuator (VOA) was placed at the input of the first filter to vary OSNR, while the average optical power incident on each detector was held constant at ≈ 1 dBm by a second VOA just before the AMZI. Error detection of the PTM RZ-QPSK was made possible by uploading the predicted AMZI output (found from a simulation) to the ED.

Conventional DQPSK is generated by precoding the baseband data at the transmitter, so that the decoded sequence in the receiver is the recovered baseband data, and in this case, PRBS. Precoding of the baseband data at the transmitter was carried out using a FPGA. In this case, the detected sequences were $2^{11}-1$ PRBS at the ED. The I and Q components of the RZ-QPSK signal were analyzed separately by adjusting the AMZI bias to $\pm \pi/4$, while baseline BPSK was optimized at an AMZI bias of π . For all signals, the optimal LA threshold was approximately the same. Since the receiver response can vary with different signal duty-cycles [32], the RZ-BPSK and RZ-QPSK signals used for the baseline measurements were generated using the Ergo-XG laser that served as the probe in the PTM RZ-QPSK experiment.

3.2 Waveguide PPD and DGD

As explained in [9], when XPM involves a polarization-scrambled signal, it is accompanied by inter-channel and intra-channel four-wave mixing that fluctuate in power depending on the relative SOPs of the pump and the probe. It was found that this polarization dependence could be mitigated through a relation between device differential group delay and pump-probe detuning (PPD) [9]. To gauge the effect of pump-induced XPM as a function of the PPD, the

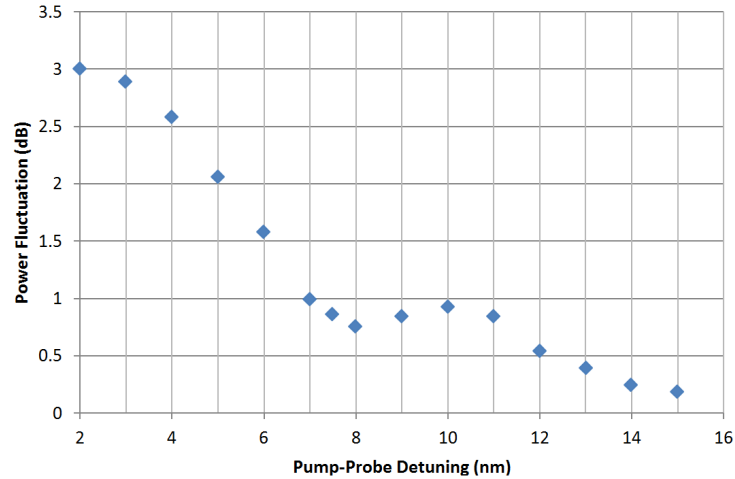


Fig. 4. Fluctuation in the filtered blue side-band of the XPM-broadened probe. The pump was launched off-axis to reduce polarization-induced fluctuations due to scrambling the probe SOP.

probe was replaced by a CW laser to simplify the experiment to wavelength conversion via XPM. The replacement was deemed necessary due to fact that the Ergo-XG laser (which functioned as the probe in the experiment) was not tunable beyond 5 nm, about 1550 nm. Moreover, a minimum PPD of ≈ 5 nm was required to minimize linear cross-talk, which was exacerbated by SPM- and XPM-induced spectral broadening in both the pump and the probe. In the wavelength conversion experiment, the CW probe was fixed at 1541 nm (limited by the bandwidth of the tunable filters in the receiver), while the RZ-OOK pump was detuned from 1543 nm to 1559 nm (limited by the useful gain bandwidth of the EDFAs), at increments of 1 nm. The coupled pump and probe powers were maintained at ≈ 21 dBm and ≈ 13 dBm, respectively. The CW probe acquired a spectral pedestal from XPM, due to its interaction with the pump. Subsequently, a 0.3-nm-OBPF was blue-shifted by 0.4 nm relative to the probe carrier to extract a portion of the XPM-induced pedestal and to suppress the probe carrier. The filtered XPM pedestal underwent PM-AM conversion in the time domain, due to its interaction with the complex transfer function of the filter. This generated a wavelength-converted 10-Gb/s RZ-OOK signal. It should be emphasized that for PTM, the filter would be centered at the probe carrier since XPM is in the same domain as the modulation format of the desired RZ-QPSK signal, as no PM-AM conversion was required. Beginning with the lowest PPD of 2 nm, the minimum-maximum (min-max) power fluctuation of the converted RZ-OOK signal were monitored on an optical spectrum analyzer (OSA) in min-max mode, as the probe SOP was scrambled at > 12 kHz. The pump launch angle was adjusted (using a polarization controller) for optimum BER, after which the min-max fluctuation was measured on the OSA. The launch angle adjustment was needed to reduce the power fluctuation of the converted RZ-OOK due to the waveguide's anisotropic nonlinearity and large PDL. The PPD was then increased and the power fluctuation of the converted RZ-OOK signal was re-measured. The resultant power fluctuation as a function of PPD is shown in Fig. 4, which demonstrates that a minimum PPD of ≈ 8 nm was required to minimize fluctuation below 1

dB. Beyond a PPD of 8 nm, the fluctuation decreased nearly monotonically. Therefore, the PPD of ~ 12 nm was chosen to be as large as possible, while staying within the useful bandwidth of the EDFAs and optical filters. Based on simplified theory presented in [9], DGD can be estimated from the minimum PPD,

$$\text{DGD} = \frac{\lambda_2^2}{c\Delta\lambda} \quad (3)$$

where $\Delta\lambda$ is the PPD and λ_2 is the probe wavelength. Given that the minimum PPD fluctuation location occurs at ≈ 8 nm, as shown in Fig. 4, the DGD is estimated to be ≈ 1 ps. Although

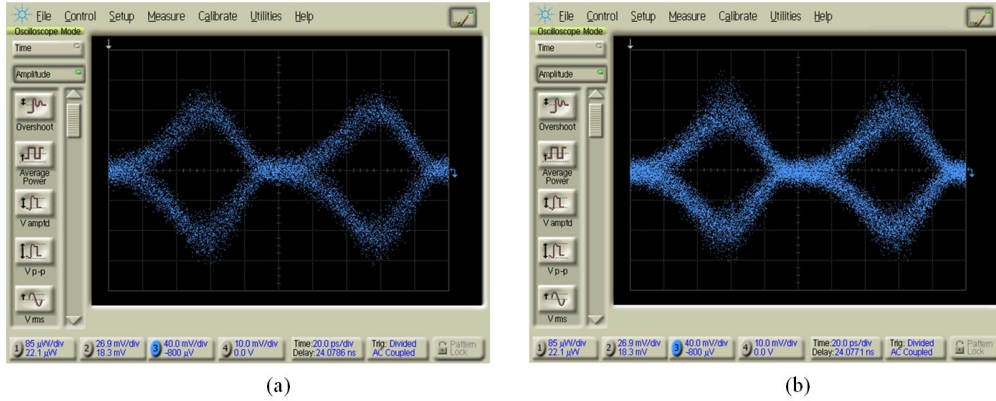


Fig. 5. (a) **Media 1**: Demonstrates PTM 20-Gb/s RZ-QPSK from 10-Gb/s RZ-BPSK and 10-Gb/s RZ-OOK. (b) **Media 2**: Demonstrates PTM RZ-QPSK *I*-component optimization when probe polarization scrambler was enabled.

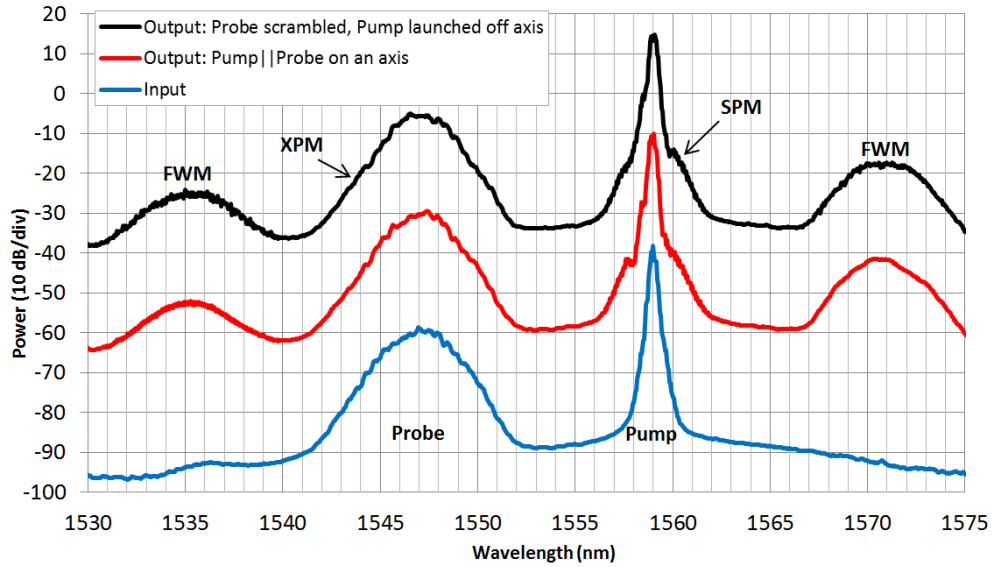


Fig. 6. Input and output Power spectra obtained at a resolution bandwidth of 0.06 nm, and for a PPD of 12 nm. The traces have been offset relative to each other for clarity. The output WDM traces exhibit pump and probe spectral broadening as well as FWM with a best conversion efficiency of ≈ -10.5 dB.

DGD is $\approx 50\%$ of the probe pulse width in the PTM RZ-QPSK experiment, it was not large enough to induce intersymbol interference (ISI) in the receiver, because after

convolution with the receiver filters and opto-electronics, the probe's FWHM pulse-width broadened to ≈ 50 ps.

3.3 Demonstrations

Attention now turns to PTM of 10-Gb/s RZ-OOK and 10-Gb/s RZ-BPSK to 20-Gb/s RZ-QPSK, utilizing PI-XPM. The single-axis condition (pump \parallel probe on an axis) was found by first aligning the probe SOP to the low-loss birefringent axis of the waveguide. The pump SOP was then aligned to the same birefringent axis by maximizing the generated FWM idler (1535nm) power at the output of the waveguide. The pump power coupled into waveguide was gradually increased from 0 to ≈ 20 dBm, to achieve the desired $\pi/2$ XPM phase shift. As the pump power was increased, the SOP of the pump and the probe were adjusted using their respective PCs to correct for pump-induced nonlinear polarization rotation. An animation of the *copolarized* PTM RZ-QPSK *I*-component is shown in Fig. 5(a) (Media 1). The PS in Fig. 3 was then enabled to achieve the case of polarization-scrambled probe, while the pump was aligned to the low-loss axis. The pump launch angle was then adjusted to reduce polarization-induced XPM, as demonstrated in the animation of Fig. 5(b) (Media 2). The angular adjustment was required to equalize the per-axis pump XPM as best as possible. The coupled probe power remained fixed at ≈ 9 dBm for all SOP conditions. The angle was expected to deviate from the symmetric launch condition of 45° found for the isotropic PCF [9], due to the linear and nonlinear anisotropies of the waveguide (Table 1).

The waveguide input and output WDM power spectra for both the pump and the probe are shown in Fig. 6 for various polarization conditions considered in the experiment. The pump and the probe exhibit spectral broadening due to SPM and XPM. A best FWM conversion efficiency, defined as the output Stokes' power relative to the output probe power, of ≈ 10.5 dB was demonstrated for pump \parallel probe on an axis. Significant, but reduced FWM conversion efficiency was observed for the case of the scrambled probe.

3.4 Theoretical receiver sensitivity

The theoretical receiver sensitivity for direct-detection of BPSK in ASE-limited transmission, with a matched optical filter and no electrical post-filtering was derived to be [33,34]

$$BER_{\text{DPSK}} = \left(\frac{1}{2} + \frac{1}{4} \frac{\Delta B}{R_s} OSNR \right) \cdot \exp \left(-2 \frac{\Delta B}{R_s} OSNR \right) \quad (4)$$

where $\Delta B/R_s$ is the ratio of the OSA resolution bandwidth to the symbol rate. Equation (4) only models OSNR degradations and is considered the best-case scenario for OSNR vs. BER. Relative to the theoretical DPSK, the experimental baseline RZ-BPSK BER performance demonstrates a penalty of ≈ 3.2 dB at 10^{-9} BER due to impairments such as pattern-dependence and AMZI frequency mismatch not considered in Eq. (4).

Theoretical receiver sensitivity for direct detection of DQPSK, in ASE-limited transmission with a matched optical filter and no electrical post-filtering was derived to be [35]

$$BER_{\text{DQPSK}} = Q(\alpha, \beta) - \frac{1}{2} e^{-[\alpha^2 + \beta^2]^{1/2}} I_0(\alpha\beta).$$

$$\begin{cases} Q(\alpha, \beta) = \int_{\beta}^{\infty} x I_0(\alpha x) e^{-(x^2 + \alpha^2)/2} dx \\ \alpha^2 = \left(1 - \frac{1}{\sqrt{2}}\right) \left(\frac{2\Delta B}{R_s} OSNR\right)^2 \\ \beta^2 = \left(1 + \frac{1}{\sqrt{2}}\right) \left(\frac{2\Delta B}{R_s} OSNR\right)^2 \end{cases} \quad (5)$$

where I_0 is the modified Bessel function of first kind, and $Q(\alpha, \beta)$ is the Marcum Q-function. Although the bit-rate of DQPSK doubled relative to DBPSK, R_s is the same for both. From Eq. (5), DQPSK demonstrates a penalty of ≈ 4.6 dB at 10^{-9} BER, relative to theoretical DPSK. Theoretically, 3 dB of the total penalty is due to I and Q components existing simultaneously within a single bit-slot, which reduces the per-channel signal power by half relative to DBPSK. The I and Q are the in-phase and quadrature sequences, after having passed through the AMZI, not to be confused with the I_0 and $Q(\alpha, \beta)$ in Eq. (5). The additional 1.6 dB is due to the direct detection scheme, in which the I and the Q channels are present in both arms of the AMZI. Like Eq. (4), Eq. (5) excludes impairments such as ISI and pattern-dependence. However, the penalty due to these impairments is collectively smaller than the ≈ 4.6 dB explained by the theory in Eq. (5).

3.5 FPGA precoder design and baseline experimental receiver sensitivity analysis

The baseline RZ-QPSK signal was precoded at the transmitter so that the detected signal would be PRBS at the EDS (Fig. 3), which was achieved using a FPGA. The FPGA design was targeted for a Xilinx ML628 Characterization Board based on a Virtex-6 HX380T FPGA.

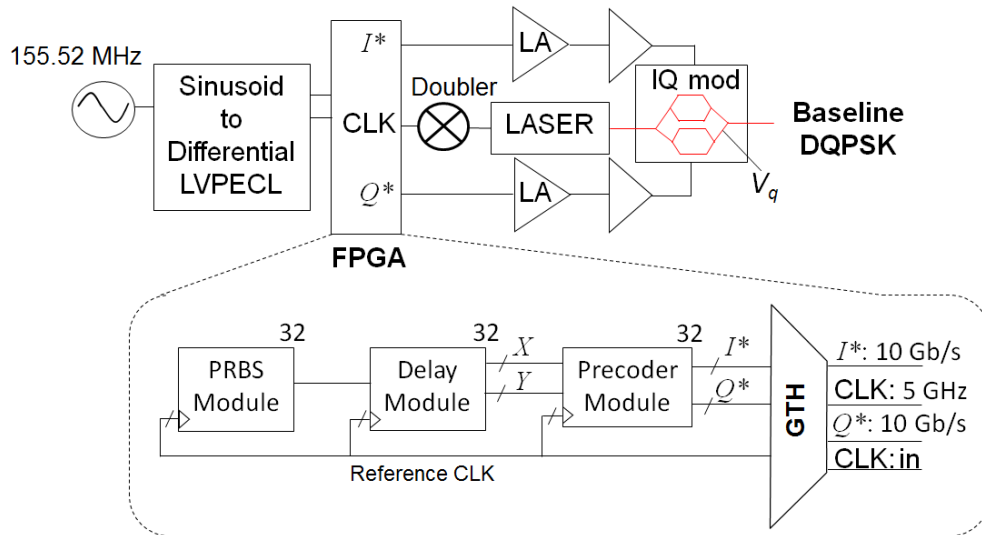


Fig. 7. Precoded-baseline RZ-QPSK transmitter setup. The Ergo-XG was used as the laser. LVPECL: low-voltage positive emitter-coupled logic, V_q : quadrature voltage.

This board supported multiple GTH serializers/deserializers that could operate with a line-rate up to 11.18 Gb/s. A low-rms-jitter external clock source was fed into the GTH tile which used a phase-locked loop to keep the RMS-jitter below 1.6 ps. The circuit specification and

design were made using the Verilog Hardware Description Language. A top-level design of the precoded baseline RZ-QPSK transmitter is shown in Fig. 7. A low-rms-jitter (< 100 fs RMS), 155.52 MHz sinusoidal, external reference clock was converted to a differential LV-PECL square wave clock and then fed to the FPGA. The clock was subsequently doubled on-board to time the internal logic at 311.04 MHz (CLK Fig. 7). Internally, 32-bit-blocks of parallel data were clocked through the system on every positive clock edge. The 32-bit-block outputs (I^* and the Q^*) of the precoder (Figs. 7 and 8) were subsequently serialized at 10 GHz by the GTH module. The 5-GHz output clock was externally doubled to drive the Ergo-XG laser at 10 GHz, which served as the pulsed source for the probe in the experiment.

The PRBS module provided a 32-bit-block of the $2^{11}-1$ PRBS at every clock cycle. The module was designed as a parallel linear feedback shift-register where new 32-bit-blocks were calculated at every clock cycle based on values in the previous and new blocks. A delay module was also built to decorrelate the *data* (X) and the *data* (Y), where *data* was defined as the $2^{11}-1$ PRBS. A dual-port memory and a 32-bit register were used to implement decorrelation (102.4 ns) between the X and Y outputs. The efficient design used only 666 slice-registers (0.14% of the total available), only 755 slice-LUTS (0.31% of the total available), and a single 36-kb block RAM (0.13% of the total available).

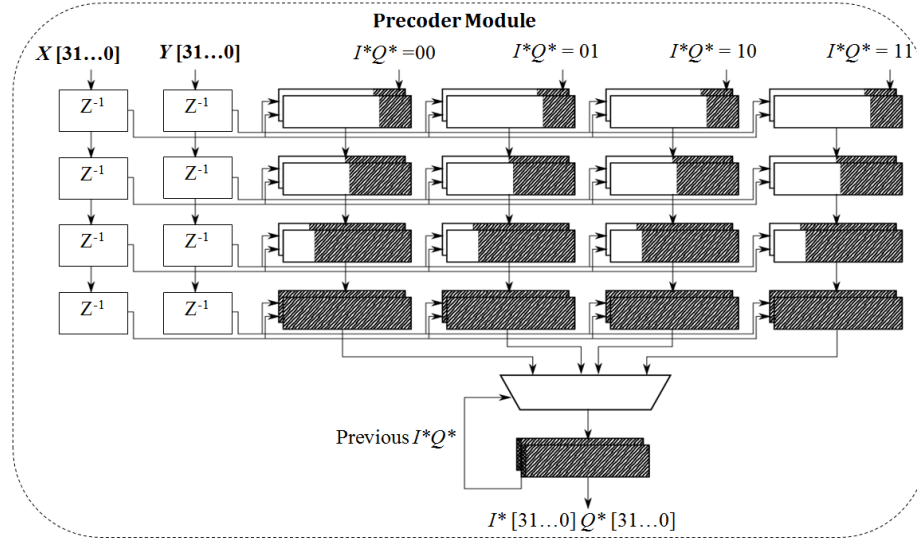


Fig. 8. Precoder module design.

For the used transmitter and receiver, the transmitter pre-coding logic took the following form [36]

$$\begin{aligned} I_n^* &= \overline{X_n Y_n I_{n-1}^*} + \overline{X_n Y_n Q_{n-1}^*} + X_n Y_n I_{n-1}^* + X_n Y_n Q_{n-1}^* \\ Q_n^* &= \overline{X_n Y_n Q_{n-1}^*} + \overline{X_n Y_n I_{n-1}^*} + X_n Y_n Q_{n-1}^* + X_n Y_n I_{n-1}^* \end{aligned} \quad (6)$$

where I^* and Q^* were the drive signals for the IQ-modulator (Fig. 7). As the precoder outputs were dependent on X and Y as well as the previously calculated I^* and Q^* bits, it created a dependency chain that would not meet the timing requirements for the basic calculations of Eq. (6). Since each 32-bit-block could not be calculated until after the previous block, an entire 32-bit-block could not be calculated in a single clock cycle. This motivated the use of an algorithm similar to a carry-select adder. All four possible initial conditions of Eq. (6) were calculated in parallel over multiple pipelined clock cycles and then the correct result was selected by a multiplexer at the end. The input X and Y blocks also propagated through a

pipeline so that the correct values were present for each stage of calculation. Figure 8 demonstrates the precoder module design. Each step in the pipeline calculates 8 of the 32 bits of the I^* and Q^* , as shown by the shaded regions in Fig. 8. A multiplexer then chooses the correct calculation based on the most significant bit of the previous I^* and Q^* blocks, and the values were then registered as the new outputs.

The precoded RZ-QPSK baseline demonstrated a penalty relative to theoretical DQPSK [Eq. (5)] of ≈ 5.6 dB at 10^{-9} BER. As previously explained, the ≈ 1 dB excess penalty is due to degradations not considered in the theoretical model, such as ISI and pattern dependence. For BER evaluation of the PTM RZ-QPSK signal, the expected sequence uploaded to the ED was predicted by first simulating the formation of RZ-QPSK via XPM for a decorrelated RZ-OOK pump and RZ-BPSK probe carrying \overline{data} and $data$, respectively. The expected I and Q signals were then found by passing the simulated PTM RZ-QPSK through an AMZI. Since the I and the Q signals generated from the PTM RZ-QPSK were not PRBS, there was a difference in their BER performances, which would normally not be a concern if both signals were PRBS.

Table 2. Received RZ-QPSK Sequence Characteristics, Illustrating Differences Between Precoded RZ-QPSK and PTM RZ-QPSK (Longest Strings of Bits are in Terms of Number of Bits, Whereas Number of Transitions Are in Terms of Consecutive State Changes)

Sequence	Length of longest string of consecutive 1s	Length of longest string of consecutive 0s	Longest string of consecutive transitions (# of transitions)
$2^{11}-1$ PRBS	11	10	6
PTM I	10	9	8
PTM Q	12	10	6

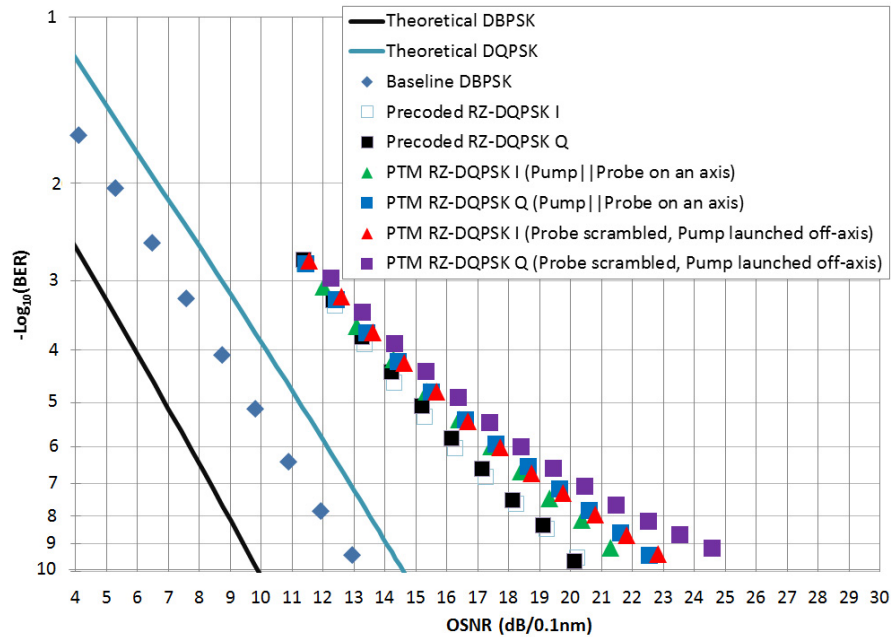


Fig. 9. Receiver sensitivity measurement results.

The difference may be attributable to the interaction of the two signals with the effective impulse response of the receiver electronics, which may be different for the lower frequency

than for the higher frequency range. Qualitative differences in I and Q signal performances can be understood through a comparison of their densities of 1s and 0s, and a count of the numbers of consecutive 01 and 10 transitions. The densities of 1s and 0s were $\approx 50\%$ for the $2^{11}-1$ PRBS and the PTM RZ-QPSK I and Q sequences. Variations in the predicted I and Q sequences become evident after evaluating the longest string of consecutive transitions. From Table 2 it is clear that the PTM RZ-QPSK Q has fewer consecutive 01 and 10 high frequency transitions than its corresponding I . Therefore, the I signal was expected to perform differently than the Q signal for all the polarization conditions considered.

According to Fig. 9, baseline precoded RZ-QPSK has a pre-amplified receiver sensitivity penalty of ≈ 7 dB relative to baseline RZ-BPSK at 10^{-9} BER, which is significantly larger than the theoretically predicted ≈ 4.6 dB [Eq. (5)]. The ≈ 2.4 dB excess penalty was due to a combination of pattern dependence, phase noise, chirp, and AMZI frequency inaccuracy. In addition, RZ-QPSK is approximately 6 times more sensitive than RZ-BPSK to AMZI frequency inaccuracy [37]. For the case of pump||probe on an axis, the PTM RZ-QPSK I signal performed ≈ 1 dB better than the Q signal at the BER metric of 10^{-9} . The difference in the I and Q signal BER performances was much less substantial at a BER metric of 10^{-3} when

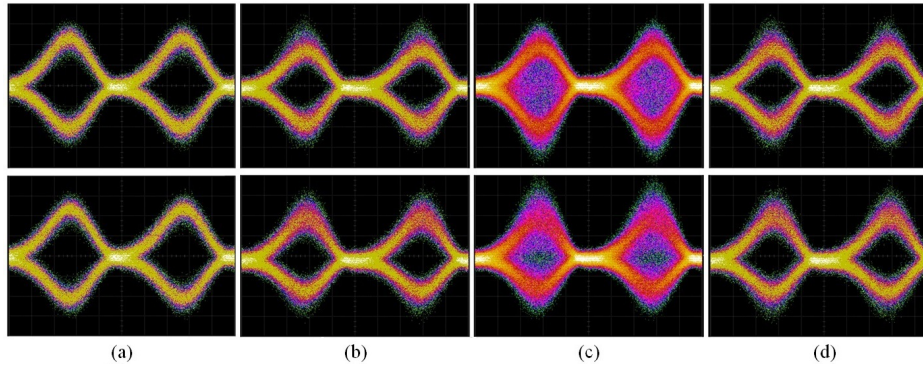


Fig. 10. Eye-diagrams of RZ-QPSK signal at OSNR > 30 dB / 0.1 nm and captured in ≈ 15 -second color-grade infinite persistence mode using a 40-GHz detector into a sampling module with a 50-GHz bandwidth. (a) baseline RZ-QPSK, and I (top), Q (bottom) when: (b) pump || probe on an axis, (c) probe polarization-scrambled and pump on an axis, (d) probe polarization-scrambled and pump launched off-axis. The polarization scrambling frequency was 12 kHz.

Table 3. Receiver Sensitivity Measurement Penalties

Case Examined	Required OSNR (dB/0.1nm) at 10^{-9} BER	Required OSNR (dB/0.1nm) at 10^{-3} BER	OSNR penalty (dB)* at 10^{-9} BER	OSNR penalty (dB)* at 10^{-3} BER
Theoretical BPSK	9.4	4.6	-10.2	-7.4
Theoretical QPSK (I and Q)	14	8.2	-5.6	-1.1
Baseline BPSK PRBS	12.8	7.1	-6.8	-4.9
Precoded baseline I (Q)	19.6(19.6)	12(12)	0(0)	0(0)
I (Q) for Pump Probe on an axis	21 (22)	12(12)	1.4(2.4)	0(0)
I (Q) for Probe Scrambled, Pump launched off-axis	22.1(24.5)	12.1(12.2)	2.5(4.9)	0.1(0.2)
I (Q) for Probe scrambled, Pump launched on-axis	synchronization loss	synchronization loss	synchronization loss	synchronization loss

*relative to precoded baseline I (Q).

ASE became the dominant corrupting mechanism, where the Q signal was only ≈ 0.1 dB worse than the I signal. The differences in the PTM RZ-QPSK I and Q signals were exacerbated for the case of the scrambled probe and the pump launched off-axis, for which the Q signal demonstrated an additional 1.5 dB penalty at 10^{-9} BER, but at 10^{-3} the penalty remained only ≈ 0.2 dB. Therefore, the Q -component suffered more from the PTM operation than the I -component as evident by the increased penalty of Q relative to I for the case of the scrambled probe and pump launched off axis. When the pump and the probe were aligned to a waveguide birefringent axis, the PTM RZ-QPSK eye-diagram demonstrated an increase in rail variances [Fig. 10(b)] relative to baseline RZ-QPSK [Fig. 10(a)]. This degradation resulted in a ≈ 1.4 dB receiver sensitivity penalty for the I signal and ≈ 2.4 dB penalty for the Q signal at a BER metric of 10^{-9} , relative to baseline RZ-QPSK (Fig. 9). For the case of the probe polarization-scrambled and the pump aligned to an axis, the eye-diagrams were closed [Fig. 10(c)] and the BER measurements exhibited synchronization loss. Due to the anisotropy of the waveguide, polarization scrambling of the RZ-BPSK probe exposed it to different axial RZ-OOK-pump-induced XPM, which was randomized as a consequence of scrambling. This caused a sufficient deviation from the ideal $\pi/2$ XPM-phase shift, and synchronization loss. The XPM randomization was reduced by launching the pump off-axis [9]. Optimization of the pump launch angle reopened the PTM RZ-QPSK I signal and Q signal eye-diagrams, as shown in Fig. 10(d), and the BER penalty reduced to ≈ 2.5 dB for the I signal and ≈ 4.9 dB for the Q signal, relative to baseline RZ-QPSK at 10^{-9} BER (Fig. 9). A portion of the penalty relative to baseline RZ-QPSK, is attributed to deviations from PRBS, chirp, residual polarization sensitivity, experimental error, as well as AMZI imperfections. Receiver sensitivity BER performance comparison for baseline, theoretical, and PTM RZ-QPSK and RZ-BPSK is summarized in Table 3.

4. Conclusion

For the first time to the authors' knowledge, 10-Gb/s RZ-OOK and polarization-scrambled 10-Gb/s RZ-BPSK to phase transmultiplexed (PTM) 20-Gb/s RZ-QPSK by polarization-insensitive XPM, has been successfully demonstrated for the first time in a passive, birefringent AlGaAs waveguide, with a DGD of ≈ 1 ps and a PDL of ≈ 1 dB. The polarization sensitivity of XPM, which was due to the anisotropy of the waveguide, was reduced by launching the pump off-axis, and using a PPD of ≈ 12 nm. Receiver sensitivity measurements were carried out to explore the performance capabilities of the PTM RZ-QPSK signal for various polarization conditions. The baseline RZ-QPSK signal was generated using a conventional IQ modulator with a FPGA based precoder. The PRBS data at the transmitter was precoded differentially to allow for PRBS recovery in the I -component and the Q -component upon reception. For the probe polarization-scrambled at 12 kHz, and the pump launched off-axis, PTM RZ-QPSK demonstrated a 10^{-9} BER receiver sensitivity penalty relative to baseline RZ-QPSK of ≈ 2.6 dB for the I -component and ≈ 4.7 dB for the Q -component. Further optimization of the waveguide structure and propagation loss could lead to PTM at much lower powers with more realistic pump and probe duty cycles.